

# Universal Signatures of Quantum Critical Points from Finite-Size Torus Spectra: A Window into the Operator Content of Higher-Dimensional Conformal Field Theories

Michael Schuler,<sup>1</sup> Seth Whitsitt,<sup>2</sup> Louis-Paul Henry,<sup>1</sup> Subir Sachdev,<sup>2,3</sup> and Andreas M. Läuchli<sup>1</sup>

<sup>1</sup>*Institut für Theoretische Physik, Universität Innsbruck, A-6020 Innsbruck, Austria*

<sup>2</sup>*Department of Physics, Harvard University, Cambridge, Massachusetts, 02138, USA*

<sup>3</sup>*Perimeter Institute for Theoretical Physics, Waterloo, Ontario N2L 2Y5, Canada*

(Dated: December 3, 2024)

The low-energy spectra of many body systems on a torus, of finite size  $L$ , are well understood in magnetically ordered and gapped topological phases. However, the spectra at quantum critical points separating such phases are largely unexplored for 2+1D systems. Using a combination of analytical and numerical techniques, we show that the low-energy torus spectrum at criticality provides a universal fingerprint of the underlying quantum field theory, with the energy levels given by universal numbers times  $1/L$ . We highlight the implications of a neighboring topological phase on the spectrum by studying the *Ising*\* transition, in the example of the toric code in a longitudinal field, and advocate a phenomenological picture that provides insight into the operator content of the critical field theory.

PACS numbers: 05.30.Rt, 11.25.Hf, 75.10.Jm, 75.40.Mg1

**Introduction** — Quantum critical points continue to attract tremendous attention in condensed matter, statistical mechanics and quantum field theory alike. Recent highlights include the discovery of quantum critical points which lie beyond the Ginzburg-Landau paradigm<sup>1,2</sup>, the striking success of the conformal bootstrap program for Wilson-Fisher fixed points<sup>3</sup>, and the intimate connection between entanglement quantities and universal data of the critical quantum field theory<sup>4-8</sup>.

A surprisingly little explored aspect in this regard is the finite (spatial) volume spectrum on numerically easily accessible geometries, such as the Hamiltonian spectrum on a 2D spatial torus at the quantum critical point<sup>9</sup>. In the realm of 1+1D conformal critical points there exists a celebrated mapping between the spectrum of scaling dimensions of the field theory in  $\mathbb{R}^2$  and the Hamiltonian spectrum on a circle (space-time cylinder:  $S^1 \times \mathbb{R}$ )<sup>10</sup>. This result is routinely used to perform accurate numerical spectroscopy of conformal critical points using a variety of numerical methods<sup>11,12</sup>. In higher dimensions the situation is less favorable: Cardy has shown<sup>13</sup> that the corresponding conformal map can be generalized to a map between  $\mathbb{R}^d$  and  $S^{d-1} \times \mathbb{R}$ . While numerical simulations in this so-called *radial quantization* geometry have been attempted at several occasions<sup>14-18</sup>, this numerical approach remains very challenging due to the curved geometry, which is inherently difficult to regularize in numerical simulations.

Due to the absence of a known relation between the scaling dimensions of the field theory and the torus energy spectra our understanding of critical energy spectra is rather limited beyond free theories<sup>19-22</sup>.

In this Letter we present a combined numerical and analytical study of the Hamiltonian torus energy spectrum of the 3D Ising conformal field theory (CFT). We demonstrate that the torus energy spectrum provides a universal fingerprint of the quantum field theory governing the critical point. It depends only on the universality class of the transition and the shape and boundary conditions of the torus, which acts as an infrared (IR) cutoff (but not on the lattice discretisation, i.e. the ultraviolet cutoff). We provide a quantitative analysis of many

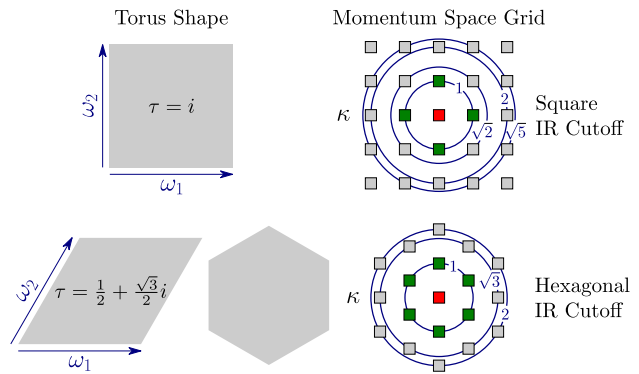


FIG. 1. The two torus geometries with 4-fold and 6-fold rotation symmetry and their momentum-space grid in the vicinity of the  $\Gamma = (0, 0)$  point. In the center of the lower row we display the Wigner-Seitz cell of the torus, highlighting the 6-fold symmetry. The momentum space variable  $\kappa$  is defined as  $\kappa = \frac{L}{2\pi}|\mathbf{k}|\tau_2$  with  $\tau = \tau_1 + i\tau_2$ ,  $L = |\omega_1| = |\omega_2|$  and  $\mathbf{k}$  a momentum of the finite-size cluster.

low-lying energy levels of the standard  $\mathbb{Z}_2$ -symmetry breaking phase transition in the 3D Ising universality class. We also advocate a phenomenological picture that provides insight into the operator content of the critical point. As an application we reveal that the torus energy spectrum of the confinement transition between the  $\mathbb{Z}_2$  topological ordered phase and the trivial (confined) phase of the Toric code (TC) in a longitudinal magnetic field can be understood as a specific combination of a subset of the fields and several boundary conditions of the standard 3D Ising universality class. Since the operator content of the partition function at criticality obviously differs from the standard 3D Ising universality class we term this transition a 3D *Ising*\* transition<sup>23-25</sup>.

**3D Ising universality class** — In order to establish the universal nature of the low-energy spectrum we study the 2+1D

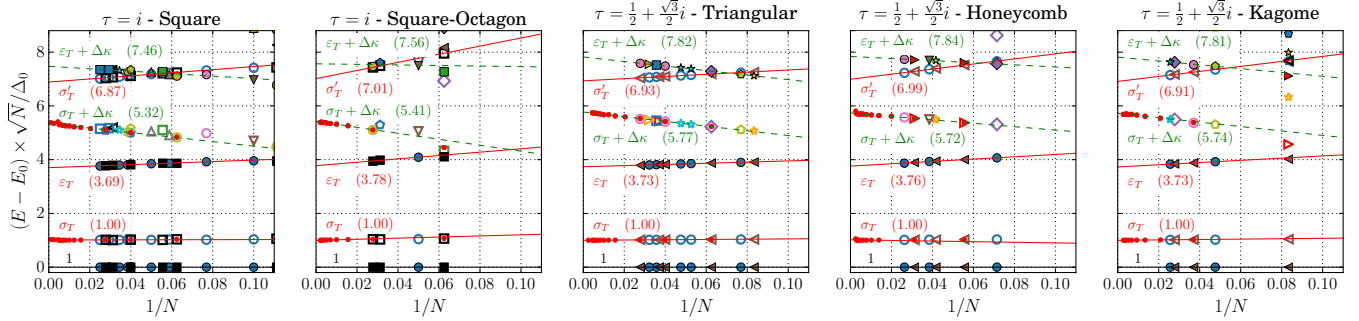


FIG. 2. Normalized low-energy torus spectrum for the Ising QFT for the modular parameters  $\tau = i$  and  $\tau = 1/2 + \sqrt{3}/2i$  obtained with ED (large symbols) and QMC (small red filled circles). Filled (empty) symbols denote  $\mathbb{Z}_2$  even (odd) levels. Linear fits in  $1/N$  for levels with  $\kappa = 0$  ( $\kappa = 1$ ) are shown by red solid (green dashed) lines (cf. color coding in Fig. 1) and the values of the fields after extrapolation to the thermodynamic limit  $1/N \rightarrow 0$  are given in parentheses. The normalization constant  $\Delta_0$  is chosen such that the first  $\mathbb{Z}_2$  odd level extrapolates to one. Remarkably, one observes a universal torus spectrum for the lattices with the same type of IR cutoff (same  $\tau$ ).

transverse field Ising (TFI) model

$$H_{\text{TFI}} = -J \sum_{\langle i,j \rangle} \sigma_i^z \sigma_j^z - h \sum_i \sigma_i^x \quad (1)$$

on five different two-dimensional Archimedean lattices<sup>26</sup> at their respective quantum critical point<sup>2728</sup>. In our finite size simulations the spatial setup is a torus whose linear extents are determined by two spanning vectors  $\omega_1$  and  $\omega_2$  (c.f. left part of Fig. 1). The finite area leads to a discrete momentum space (c.f. right part of Fig. 1) and is equivalent to an infrared (IR) cutoff in the field theory. The use of a lattice model on the other hand leads to an ultraviolet (UV) cutoff in the form of a Brillouin zone. In the following we will only consider tori with  $L = |\omega_1| = |\omega_2|$  and two different choices of the modular parameter  $\tau = \omega_2/\omega_1$ :  $\tau = i$  ( $\tau = 1/2 + \sqrt{3}/2i$ ) corresponding to a square (hexagonal) symmetry. The square and square-octagon (triangular, honeycomb and kagome) lattices are simulated using a square (hexagonal) IR-cutoff geometry to preserve the microscopic  $C_4$  ( $C_6$ ) point group symmetry in the IR.

In a first step we have calculated the low-energy spectrum of the Hamiltonian Eq. (1) using exact diagonalization (ED) in all symmetry sectors on finite samples with up to  $N = 40$  spins in total. The spectrum can be divided into  $\mathbb{Z}_2$  even and odd sectors (spin-flip symmetry), combined with irreducible representations of the lattice space group. In the paramagnetic phase at large  $h/J$  one finds a unique  $\mathbb{Z}_2$  even ground state in the fully symmetric spatial representation, with a finite gap above the ground state. At small  $h/J$  one finds two quasi-degenerate ground states in the  $\mathbb{Z}_2$  even and odd sector respectively (both in the symmetric spatial representation), again with a finite gap above the ground state. At the quantum critical point ( $h/J$ )<sub>c</sub> however the low-lying spectrum collapses as  $1/\sqrt{N} \sim 1/L$ , i.e. it exhibits a mass spectrum with the mass scale set by the IR cutoff. To get rid of this scaling we will multiply the excitation gaps with  $\sqrt{N}$  in the following and will call that the spectrum. In Fig. 2 we display the finite size spectra at the Ising critical point for all five different lattices in the zero momentum sector  $\Gamma = (0, 0)$ , as well

as the first momentum away from the  $\Gamma$  point ( $\kappa = 1$  in the right part of Fig. 1). Since the speed of light is not known at this stage, the spectrum for each lattice has been globally rescaled such that the extrapolated energy of the first excited level (which is  $\mathbb{Z}_2$  odd and spatially symmetric) is set to one. One nicely observes that the critical energy spectra of lattices with the same type of IR cutoff  $\tau$  (the two leftmost panels and the three rightmost panels) agree to rather high precision with each other, when taking  $1/N$  finite-size corrections into account. In order to corroborate the extrapolations based on ED we performed extensive Quantum Monte Carlo (QMC) simulations<sup>27</sup> of the transverse field Ising model at the critical point for all five lattices. Based on imaginary time spin-spin correlations it is possible to access the finite size gaps on lattices up to  $N = 30 \times 30$  lattice sites. These data points (red small filled circles) in Fig. 2 reproduce the ED data where available, and allow us to confirm and sharpen the precision of the extrapolated energy spectrum. Based on the quantum numbers of the first few low-lying energy levels we choose to label them as torus analogues of the spectrum of scaling dimensions of the 3D Ising CFT:  $\sigma_T$  and  $\sigma'_T$  refer to the first two levels in the  $\mathbb{Z}_2$  odd sector in the spatially symmetric representation, while  $\epsilon_T$  is the first excited state (above the vacuum 1) in the  $\mathbb{Z}_2$  even and spatially symmetric sector. The “... +  $\Delta\kappa$ ” label refers to levels at the first momentum away from the  $\Gamma$  point,  $\kappa = 1$ . These levels are four-fold degenerate on the square torus, while they are six-fold degenerate for the hexagonal torus.

*ε-expansion* — We also compute the energy levels using  $\epsilon$ -expansion. Our starting point is  $\phi^4$  theory, which we define by the Hamiltonian density

$$\mathcal{H} = \int d^d x \left[ \frac{1}{2} \Pi^2 + \frac{1}{2} (\nabla \phi)^2 + \frac{s}{2} \phi^2 + \frac{u}{4!} \phi^4 \right] \quad (2)$$

in  $d$  dimensions with the equal-time commutator  $[\phi(x, t), \Pi(x', t)] = i\delta^d(x - x')$ , and specialize to the critical point,  $s = s_c$ ,  $u = u^*$ . We generalize the two-dimensional torus to arbitrary dimension by taking  $d/2$  copies of the desired torii in Fig. 1, so that all spatial point-

symmetries are preserved during the calculation and no extra length scales are introduced.

Our approach to the critical theory in a finite volume originated from Lüscher<sup>29</sup>, and was extended to deal with finite size criticality in classical systems by others<sup>30,31</sup>. The key observation is that the zero mode of the field generates incurable infrared divergences in perturbation theory, so it must be separated and treated non-perturbatively. In the context of the finite-size spectrum, this can be understood from Eq. (2) by noticing that the Gaussian theory at  $s = 0$  does not contain any potential term for the zero mode, giving a continuous spectrum, whereas any finite  $u$  will confine the zero mode producing a discrete spectrum. Therefore, the correct perturbative approach is to treat the momentum of the zero mode at the same order as its interactions.

By splitting the fields in Eq. (2) and proper normalization of the zero-mode terms the Hamiltonian can be decomposed into a quadratic part  $\mathcal{H}_0$  describing the Fock spectrum of the finite-momentum modes, and an interaction part  $V$  containing all zero-mode contributions and non-linearities.

At zeroth order, our states are given by finite momentum Fock states multiplied by arbitrary functionals of the zero mode, so these states are infinitely degenerate. We then derive an effective Hamiltonian within each degenerate subspace using a perturbation method due to C. Bloch<sup>32</sup>. This effective Hamiltonian acts in a degenerate subspace, but its eigenvalues correspond to the exact eigenvalues of the original Hamiltonian to desired order. It turns out, that the effective Hamiltonians take the form of a strongly-coupled oscillator with coefficients depending on the degenerate subspaces. The coefficients of the more complicated expansion for the energy levels (expansion in  $\epsilon^{1/3}$ ) can be found in<sup>33</sup>. In addition, the effective Hamiltonian will couple different Fock states with the same energy and momentum whenever possible, leading to off-diagonal terms. These off-diagonal terms were computed numerically from the unperturbed wave-function.

In Fig. 3 we show the universal torus spectrum for the two choices of  $\tau$  obtained from  $\epsilon$ -expansion and compare it to numerical results from ED/QMC<sup>34</sup> normalized by the speed of light  $c$ <sup>35,36</sup>. We observe a remarkable agreement between the two different methods. This further strengthens the interpretation of the torus spectra as universal fingerprint of the critical field theory. The larger discrepancies between numerical and  $\epsilon$ -expansion data for some higher levels in the spectrum may result from the extrapolation to the thermodynamic limit using only ED data with strong finite-size effects, especially for  $\kappa > 0$ <sup>37</sup>.

**2+1D Ising\* universality class** — In this section we are investigating the confinement transition of a  $\mathbb{Z}_2$  spin liquid. Such a topological quantum phase transition is characterized by the lack of any local order parameters.  $\mathbb{Z}_2$  spin liquids are characterized by the presence of two bosons, the  $e$  and  $m$  particles. These fractionalized particles can only be created in pairs and obey mutual anyonic statistics. The confinement transition can then be driven by condensing either the  $e$  or the  $m$  particles. Without loss of generality, we will consider the condensation of the  $m$  particles and call it's corresponding field  $\phi$ . The critical theory turns out to be *Ising\**:  $\phi$  can only

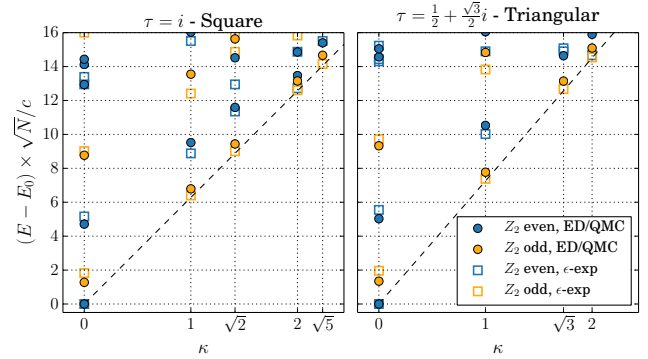


FIG. 3. Universal torus spectra for the Ising QFT for the modular parameters  $\tau = i$  (left panel) and  $\tau = 1/2 + \sqrt{3}/2i$  (right panel). Full symbols denote numerical results obtained by ED or QMC (the lowest  $Z_2$  odd levels), while empty symbols denote the  $\epsilon$ -expansion results. The dashed line shows a dispersion according to the speed of light.

be created in pairs, so the effective Lagrangian must be even in a real field  $\phi$ , implying we should only include  $\mathbb{Z}_2$  even states in a critical Ising theory. In addition,  $\phi$  and  $-\phi$  are physically indistinguishable, and so both periodic and anti-periodic boundary conditions have to be considered. We want to emphasize that this mapping is independent of any specific microscopic lattice model and should hold generically between universal theories and their topological counterparts.

As a microscopic model illustrating this transition we study the critical energy spectrum of the Toric Code Hamiltonian perturbed by a longitudinal field<sup>38–42</sup>:

$$H_{TC} = -J \sum_s A_s - J \sum_p B_p - h \sum_i \sigma_i^x \quad (3)$$

$$A_s = \prod_{i \in s} \sigma_i^x, \quad B_p = \prod_{i \in p} \sigma_i^z$$

The  $\sigma_i$  describe  $S = 1/2$ -spins on the  $2N$  edges of a square lattice,  $p$  denotes a plaquette and  $s$  a star on the lattice. All  $A_s$  and  $B_p$  commute with each other and so the model can be solved analytically for  $h = 0$  by setting  $A_s = 1 \forall s$  and  $B_p = 1 \forall p$ <sup>43</sup>. On a torus the ground state manifold is, however, four-fold degenerate and can be characterized by the eigenvalues  $\pm 1$  of Wilson loops winding around the torus. An  $e$  ( $m$ ) particle is described by setting  $A_s = -1$  ( $B_p = -1$ ) on a star (plaquette). The longitudinal field introduces a dispersion for the  $m$  particles which finally condense and drive the phase transition at  $h = h_c$  by confinement of the  $e$  particles<sup>23–25,38</sup>.

The above considerations regarding the relationship between Ising and Ising\* QFT can be made very explicit for the Toric Code. The Toric Code Eq. (3) in the sector without  $e$  particles ( $A_s = 1 \forall s$ ) can be exactly mapped to an even TFI model on the dual square lattice with  $N$  sites, where only the even spin-flip sector is present<sup>38,44,45</sup>. The groundstate manifold, described by the eigenvalues of the Wilson loops, maps to both, periodic and anti-periodic boundary conditions of the Ising model<sup>46</sup>. In the following we will make use of this mapping to compute the finite-size torus spectrum of the *Ising\** transition for  $\tau = i$  using ED.

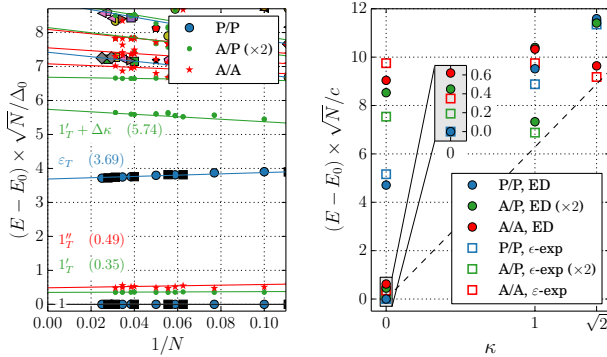


FIG. 4. Universal torus spectra for the *Ising*\* QFT and the modular parameters  $\tau = i$ . The labels A/P etc. denote the boundary conditions along the two directions of the torus, where P(A) means (anti-)periodic. Left: Normalized low-energy spectrum from ED with the same normalization constant  $\Delta_0$  as in Fig. 2. The levels in the P/P sector are the  $\varepsilon_T(+\Delta\kappa)$  levels from the TFI spectrum. A very remarkable feature are the four very low-lying levels which govern the four-fold degenerate groundstate manifold in the deconfined phase. See Fig. 2 for further details. Right: Full symbols denote numerical results obtained by ED, while empty symbols denote  $\epsilon$ -expansion results. The dashed line shows a dispersion with the speed of light. The inset is a zoom into the four lowest levels. See Fig. 3 for further details.

In the left part of Fig. 4 we present the low-energy finite-size spectrum of the *Ising*\* transition obtained with ED simulations. The spectrum is rescaled with the same factor  $\Delta_0$  as in Fig. 2 such that they can be easily compared. The relationship between the critical *Ising* and *Ising*\* theories results in the fact that the levels called  $\varepsilon_T(+\Delta\kappa)$  in Fig. 2 are identically present in the *Ising*\* spectrum (c.f. P/P levels in Fig. 4). The most remarkable feature, however, is the presence of very low-

lying levels in the spectrum. They arise from the groundstate manifold in the spin-liquid phase, where their splitting exponentially scales to zero with  $L$ . At criticality they, however, scale as  $1/\sqrt{N}$  as the entire low-energy spectrum. The small relative splitting of the four lowest levels is surprisingly small. The right panel of Fig. 4 shows a comparison of the universal torus spectrum for an *Ising*\* transition obtained with ED and  $\epsilon$ -expansion similar to Fig. 3<sup>47</sup>. A zoom into the conspicuous low-energy levels is shown in the inset. Again we observe a decent agreement of the different methods fortifying the idea of a universal torus spectrum also for the *Ising*\* transition.

*Conclusions* — We have convincingly shown that the torus energy spectrum provides a characteristic fingerprint of the conformal field theory and its operator content governing a quantum critical point in 2+1D. Using the numerical and analytical technology presented in this paper it will be possible to inspect and chart the characteristic spectrum of more complex quantum critical points, such as  $O(N)$  Wilson-Fisher fixed points, Gross-Neveu-Yukawa type phase transitions in interacting Dirac fermion models<sup>48,49</sup> or designer Hamiltonians displaying deconfined criticality<sup>2</sup>.

A.M.L. thanks R.C. Brower, J.L. Cardy and A.W. Sandvik for discussions. L.-P.H. and M.S. acknowledge support through the Austrian Science Fund SFB FoQuS (F-4018). S.W. and S.S. are supported by the U.S. NSF under Grant DMR-1360789. The computational results presented have been achieved in part using the Vienna Scientific Cluster (VSC). This work was supported by the Austrian Ministry of Science BMWF as part of the UniInfrastrukturprogramm of the Focal Point Scientific Computing at the University of Innsbruck. Research at Perimeter Institute is supported by the Government of Canada through Industry Canada and by the Province of Ontario through the Ministry of Research and Innovation. This research was supported in part by the National Science Foundation under Grant No. NSF PHY11-25915.

---

<sup>1</sup> T. Senthil, A. Vishwanath, L. Balents, S. Sachdev, and M. P. A. Fisher, “Deconfined Quantum Critical Points,” *Science* **303**, 1490–1494 (2004).

<sup>2</sup> A. W. Sandvik, “Evidence for deconfined quantum criticality in a two-dimensional Heisenberg model with four-spin interactions,” *Phys. Rev. Lett.* **98**, 227202 (2007), arXiv:0611343 [cond-mat].

<sup>3</sup> S. El-Showk, M. F. Paulos, D. Poland, S. Rychkov, D. Simmons-Duffin, and A. Vichi, “Solving the 3D Ising model with the conformal bootstrap,” *Phys. Rev. D* **86**, 025022 (2012), arXiv:1403.4545; “Solving the 3d Ising Model with the Conformal Bootstrap II.  $c$ -Minimization and Precise Critical Exponents,” *J. Stat. Phys.* **157**, 869–914 (2014), arXiv:1403.4545v2.

<sup>4</sup> C. Holzhey, F. Larsen, and F. Wilczek, “Geometric and renormalized entropy in conformal field theory,” *Nucl. Phys. B* **424**, 443–467 (1994).

<sup>5</sup> P. Calabrese and J. Cardy, “Entanglement entropy and quantum field theory,” *J. Stat. Mech. Theor. Exp.* **2004**, P06002 (2004).

<sup>6</sup> A. M. Läuchli, “Operator content of real-space entanglement spectra at conformal critical points,” *ArXiv e-prints* (2013), arXiv:1303.0741.

<sup>7</sup> A. B. Kallin, K. Hyatt, R. R. P. Singh, and R. G. Melko, “Entanglement at a Two-Dimensional Quantum Critical Point: A Numerical Linked-Cluster Expansion Study,” *Phys. Rev. Lett.* **110**, 135702 (2013).

<sup>8</sup> P. Bueno, R. C. Myers, and W. Witczak-Krempa, “Universality of Corner Entanglement in Conformal Field Theories,” *Phys. Rev. Lett.* **115**, 021602 (2015).

<sup>9</sup> In a corresponding classical statistical mechanics language, we are discussing the spectrum of the logarithm of the transfer matrix in the limit of an infinitely long square (or hexagonal) rod (c.f. left part of Fig. 1). The transfer matrix acts along the infinite rod direction.

<sup>10</sup> J. L. Cardy, “Conformal invariance and universality in finite-size scaling,” *J. Phys. A. Math. Gen.* **17**, L385–L387 (1984).

<sup>11</sup> A. Feiguin, S. Trebst, A. W. W. Ludwig, M. Troyer, A. Kitaev, Z. Wang, and M. H. Freedman, “Interacting Anyons in Topological Quantum Liquids: The Golden Chain,” *Phys. Rev. Lett.* **98**, 160409 (2007).

<sup>12</sup> H. Suwa and S. Todo, “Generalized Moment Method for Gap Estimation and Quantum Monte Carlo Level Spectroscopy,” *Phys.*

*Rev. Lett.* **115**, 080601 (2015), arXiv:1402.0847.

<sup>13</sup> J. L. Cardy, “Universal amplitudes in finite-size scaling: generalisation to arbitrary dimensionality,” *J. Phys. A. Math. Gen.* **18**, L757–L760 (1985).

<sup>14</sup> F. C. Alcaraz and H. J. Herrmann, “Numerical difficulties in obtaining 3D critical exponents from Platonic solids,” *J. Phys. A. Math. Gen.* **20**, 5735–5736 (1987).

<sup>15</sup> M. Weigel and W. Janke, “Universal amplitude-exponent relation for the Ising model on sphere-like lattices,” *Europhys. Lett.* **51**, 578–583 (2000), arXiv:0008292 [cond-mat].

<sup>16</sup> Y. Deng and H. W. J. Blöte, “Conformal Invariance of the Ising Model in Three Dimensions,” *Phys. Rev. Lett.* **88**, 190602 (2002).

<sup>17</sup> R. C. Brower, G. T. Fleming, and H. Neuberger, “Lattice radial quantization: 3D Ising,” *Phys. Lett. B* **721**, 299–305 (2013), arXiv:1212.6190v1.

<sup>18</sup> R. C. Brower, G. Fleming, A. Gasbarro, T. Raben, C.-I. Tan, and E. Weinberg, “Quantum Finite Elements for Lattice Field Theory,” *ArXiv e-prints* (2016), arXiv:1601.01367.

<sup>19</sup> M. Henkel, “Universal ratios of scaling amplitudes in the Hamiltonian limit of the 3D Ising model,” *J. Phys. A. Math. Gen.* **19**, L247–L249 (1986); “Finite size scaling and universality in the (2+1)D Ising model,” *J. Phys. A. Math. Gen.* **20**, 3969–3981 (1987).

<sup>20</sup> C. J. Hamer, “Finite-size scaling in the (2+1)D Ising model,” *J. Phys. A. Math. Gen.* **16**, 1257–1266 (1983); “The (2+1)D Ising model on a triangular lattice,” *J. Phys. A. Math. Gen.* **19**, 423–435 (1986); “Finite-size scaling in the transverse Ising model on a square lattice,” *J. Phys. A. Math. Gen.* **33**, 6683–6698 (2000), arXiv:0007063 [cond-mat].

<sup>21</sup> Y. Nishiyama, “Bound-state energy of the three-dimensional Ising model in the broken-symmetry phase: Suppressed finite-size corrections,” *Phys. Rev. E* **77**, 051112 (2008), arXiv:0804.1586.

<sup>22</sup> S. Dusuel, M. Kamfor, K. P. Schmidt, R. Thomale, and J. Vidal, “Bound states in two-dimensional spin systems near the Ising limit: A quantum finite-lattice study,” *Phys. Rev. B* **81**, 064412 (2010), arXiv:0912.1463.

<sup>23</sup> R. A. Jalabert and S. Sachdev, “Spontaneous alignment of frustrated bonds in an anisotropic, three-dimensional Ising model,” *Phys. Rev. B* **44**, 686–690 (1991).

<sup>24</sup> S. Sachdev and M. Vojta, “Translational symmetry breaking in two-dimensional antiferromagnets and superconductors,” *J. Phys. Soc. Jpn.* **69**, Supp. B, 1 (1999), arXiv:cond-mat/9910231.

<sup>25</sup> T. Senthil and M. P. A. Fisher, “ $Z_2$  gauge theory of electron fractionalization in strongly correlated systems,” *Phys. Rev. B* **62**, 7850–7881 (2000).

<sup>26</sup> See Supplemental Material for a definition of the Archimedean lattices.

<sup>27</sup> H. W. J. Blöte and Y. Deng, “Cluster Monte Carlo simulation of the transverse Ising model,” *Phys. Rev. E* **66**, 066110 (2002).

<sup>28</sup> We have computed the critical point for the Square-Octagon lattice as  $(h/J)_c = 2.087(7)$  using a continuous-time QMC algorithm similar to that of<sup>27</sup>.

<sup>29</sup> M. Lüscher, “A new method to compute the spectrum of low-lying states in massless asymptotically free field theories,” *Phys. Lett. B* **118**, 391 – 394 (1982).

<sup>30</sup> E. Brézin and J. Zinn-Justin, “Finite size effects in phase transitions,” *Nucl. Phys. B* **257**, 867 – 893 (1985).

<sup>31</sup> J. Rudnick, H. Guo, and D. Jasnow, “Finite-size scaling and the renormalization group,” *J. Stat. Phys.* **41**, 353–373 (1985).

<sup>32</sup> C. Bloch, “Sur la théorie des perturbations des états liés,” *Nucl. Phys.* **6**, 329 – 347 (1958).

<sup>33</sup> L. Skála, J. Cízek, and J. Zamastil, “Strong coupling perturbation expansions for anharmonic oscillators. Numerical results,” *J. Phys. A. Math. Gen.* **32**, 5715 (1999).

<sup>34</sup> See Supplemental Material for a listing of the complete low-energy torus spectra for the Ising transition from numerics and  $\epsilon$ -expansion.

<sup>35</sup> A. Sen, H. Suwa, and A. W. Sandvik, “Velocity of excitations in ordered, disordered, and critical antiferromagnets,” *Phys. Rev. B* **92**, 195145 (2015), arXiv:1505.02535.

<sup>36</sup> See Supplemental Material for the details on the determination of  $c$ .

<sup>37</sup> For further studies it is worth noticing that  $\epsilon$ -expansion tends to overestimate the  $\kappa = 0$  levels while levels with  $\kappa > 0$  are commonly underestimated.

<sup>38</sup> S. Trebst, P. Werner, M. Troyer, K. Shtengel, and C. Nayak, “Breakdown of a Topological Phase: Quantum Phase Transition in a Loop Gas Model with Tension,” *Phys. Rev. Lett.* **98**, 070602 (2007), arXiv:0609048 [cond-mat].

<sup>39</sup> J. Vidal, S. Dusuel, and K. P. Schmidt, “Low-energy effective theory of the toric code model in a parallel magnetic field,” *Phys. Rev. B* **79**, 033109 (2009).

<sup>40</sup> I. S. Tupitsyn, A. Kitaev, N. V. Prokof’ev, and P. C. E. Stamp, “Topological multicritical point in the phase diagram of the toric code model and three-dimensional lattice gauge Higgs model,” *Phys. Rev. B* **82**, 085114 (2010), arXiv:0804.3175v1.

<sup>41</sup> S. Dusuel, M. Kamfor, R. Orús, K. P. Schmidt, and J. Vidal, “Robustness of a Perturbed Topological Phase,” *Phys. Rev. Lett.* **106**, 107203 (2011), arXiv:1012.1740.

<sup>42</sup> F. Wu, Y. Deng, and N. Prokof’ev, “Phase diagram of the toric code model in a parallel magnetic field,” *Phys. Rev. B* **85**, 195104 (2012).

<sup>43</sup> A. Y. Kitaev, “Fault-tolerant quantum computation by anyons,” *Ann. Phys.* **303**, 2–30 (2003).

<sup>44</sup> A. Hamma and D. A. Lidar, “Adiabatic Preparation of Topological Order,” *Phys. Rev. Lett.* **100**, 030502 (2008), arXiv:0607145 [quant-ph].

<sup>45</sup> L. Carr, ed., *Understanding Quantum Phase Transitions*, Condensed Matter Physics, Vol. 20103812 (CRC Press, 2010).

<sup>46</sup> See Supplemental Material for a detailed discussion of the mapping.

<sup>47</sup> See Supplemental Material for a listing of the complete low-energy torus spectra for the Ising\* transition from numerics and  $\epsilon$ -expansion.

<sup>48</sup> L. Wang, P. Corboz, and M. Troyer, “Fermionic quantum critical point of spinless fermions on a honeycomb lattice,” *New J. Phys.* **16**, 103008 (2014).

<sup>49</sup> Z.-X. Li, Y.-F. Jiang, and H. Yao, “Fermion-sign-free Majorana-quantum-Monte-Carlo studies of quantum critical phenomena of Dirac fermions in two dimensions,” *New J. Phys.* **17**, 085003 (2015).

## Supplemental Material: Universal Signatures of Quantum Critical Points from Finite-Size Torus Spectra

### Appendix A: Lattice geometries

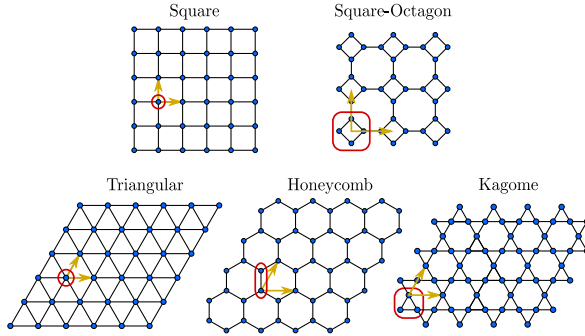


FIG. 5. The different lattice geometries used for the TFI model. The red boxes indicate the lattice basis cells, the arrows mark the Bravais vectors. The square and square-octagon lattices obey a  $C_4$  rotational symmetry, the triangular, honeycomb and kagome lattices a  $C_6$  rotational symmetry.

### Appendix B: Mapping the perturbed Toric Code onto the transverse field Ising model

In this section, we demonstrate an exact mapping of the charge-free sector of the Toric Code model perturbed by a longitudinal field to a transverse field Ising model with only even states under spin-inversion. Such a mapping has already been used in previous studies of the Toric Code<sup>38,44,45</sup>, here we will additionally show that the different groundstate sectors of the Toric Code result in different boundary conditions of the transverse field Ising model.

The Hamiltonian of the Toric Code in a longitudinal field is

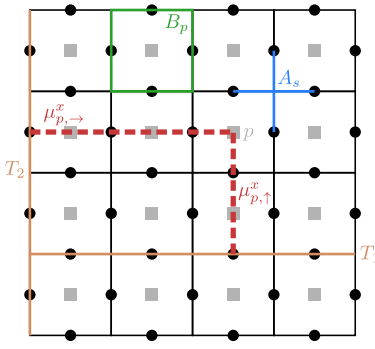


FIG. 6. The Toric Code on a torus. Black dots show the positions of the Toric Code variables  $\sigma_i^{x,z}$ , grey squares the dual lattice for the variables  $\mu_p^{x,z}$ .  $T_{1,2}$  depict a choice of the two incontractible loops winding around the torus. See text for further details.

given by

$$H = -J \sum_s A_s - J \sum_p B_p - h \sum_i \sigma_i^x \quad (B1)$$

$$A_s = \prod_{i \in s} \sigma_i^x, \quad B_p = \prod_{i \in p} \sigma_i^z \quad (B2)$$

where the  $\sigma_i$  describe spins on the links of a square lattice,  $p$  denotes a plaquette and  $s$  a star on this lattice. All  $A_s$  and  $B_p$  commute with each other and thus the GS of the Hamiltonian for  $h = 0$  can be found by setting  $A_s = 1 \forall s$  and  $B_p = 1 \forall p$ . On a torus, however, not all of the  $A_s$  and  $B_p$  are linearly independent, as  $\prod_s A_s = 1$  and  $\prod_p B_p = 1$ , leading to a 4-fold degenerate groundstate manifold. This groundstate manifold can be distinguished by the expectation values of the Wilson loop operators  $t_{1,2} = \prod_i \sigma_i^x$  where the paths wind around the torus along two non-contractible loops through the centers of the edges of the lattice (e.g. parallel to  $T_{1,2}$  in Fig. 6).

To perform the mapping to a transverse field Ising model we first note, that  $A_s$  and  $t_{1,2}$  are still conserved for  $h \neq 0$ , when the longitudinal field is turned on. So, we consider the charge-free sector,  $A_s = 1 \forall s$ , which describes the low-energy physics even at criticality, and define the new variables

$$\mu_p^z = B_p \quad (B3)$$

$$\mu_{p,→(↑)}^x = \prod_{i \in c_{p,→(↑)}} \sigma_i^x \quad (B4)$$

on each site  $p$  of the dual lattice (center of plaquette  $p$ )<sup>44</sup>. We choose two incontractible paths  $T_{1,2}$  in  $\hat{x}(\hat{y})$  direction along the lattice. The path  $c_{p,→(↑)}$  is then a straight path from  $T_{2(1)}$  to the site  $p$  in  $\hat{x}(\hat{y})$ -direction along the dual lattice (cf. Fig. 6). It is straightforward to show that these variables fulfill the Pauli-Algebra  $\{\mu_p^x, \mu_p^z\} = 0, (\mu_p^x)^2 = 1$  and that

$$\sigma_i^x(\hat{x}) = \mu_{p(i),↑}^x \mu_{p(i)-\hat{y},↑}^x \quad (B5)$$

$$\sigma_i^x(\hat{y}) = \mu_{p(i),→}^x \mu_{p(i)-\hat{x},→}^x \quad (B6)$$

where  $\sigma_i^x(\hat{x}(\hat{y}))$  describes a Pauli operator on a link in  $\hat{x}(\hat{y})$ -direction on the lattice.

With this, the TC eventually maps onto the well-known TFI model

$$H_{TFI} = -h \sum_{\langle p,q \rangle} \mu_p^x \mu_q^x - J_p \sum_p \mu_p^z + \text{const.} \quad (B7)$$

on the dual lattice and  $A_s = 1 \forall s$ , as it was imposed.

The resulting transverse field Ising model Eq. (B7) is invariant under global spin-inversion  $\mathcal{I} = \prod_p \mu_p^z$ . From Eq. (B3) it immediately follows that

$$\mathcal{I} = \prod_p B_p = 1 \quad (B8)$$

where the last equality is always satisfied on a torus and so the Toric Code maps to an *even* transverse field Ising model.

Let us finally apply the mapping on the different groundstate sectors characterized by the eigenvalues of  $t_{1,2}$ . Using

Eq. (B5) and Eq. (B6) it follows that

$$t_1 = \prod_{p=0}^{L-1} \mu_{(p,j)}^x \mu_{(p+1,j)}^x = \mu_{(0,j)}^x \mu_{(L,j)}^x \quad (\text{B9})$$

where the index  $(p, j)$  labels the position  $p\hat{x} + j\hat{y}$  on the dual lattice and  $L$  is the linear extend of the torus. An equivalent relation can be computed for  $t_2$ . The different ground-state sectors of the Toric Code therefore map onto periodic and antiperiodic boundary conditions of the transverse field Ising model for both directions around the torus.

### Appendix C: Speed of light from QMC

For each lattice, in order to extract the speed of light  $c$ , we proceed as follows. We first extract with QMC the energies  $E_L^{\sigma_T}(\kappa)$  of the lowest  $\mathbb{Z}_2$  odd levels at a given system size  $L$ . We then extrapolate those to the thermodynamic limit  $E^{\sigma_T}(\kappa)$ . We finally fit a line  $E^{\sigma_T}(\kappa) = \delta E + c \cdot \kappa$  to this extrapolated data, in the interval  $[\kappa_{\min}, \kappa_{\max}]$ <sup>35</sup>. Since we expect the levels at small momenta to be affected by the periodic boundary conditions, we take  $\kappa_{\min} > 0$ . For large momenta, the finite-size curvature effects render the thermodynamic-limit extrapolation ill-defined, and therefore one has to introduce an ultraviolet cutoff  $\kappa_{\max}$ . There is ambiguity in the choice of  $\kappa_{\min}$  and  $\kappa_{\max}$ , but for all *reasonable* choices (*i.e.* so that enough points lie within the linear regime in this interval), one gets a value for  $c$  with a fitting asymptotic standard error of less than 0.5%. However, the value of  $c$  thus obtained varies by about 1% (2%) for the square and triangular lattices (square-octagon, honeycomb and kagome lattices) across the various choices of fitting intervals. This leads to the speed of light estimates given in Tab. I.

Lattice	$c/J$	(prev. works)
Square	$3.323 \pm 0.033$	$3.01 \pm 0.09^{20}$
Square-Octagon	$5.126 \pm 0.103$	
Triangular	$2.047 \pm 0.020$	
Honeycomb	$2.923 \pm 0.058$	
Kagome	$2.013 \pm 0.040$	

TABLE I. Speed of light for each lattice geometry, from QMC.

**Appendix D: Complete low-energy spectrum for Ising CFT with modular parameter  $\tau = i$** 

$\tau = i$	$\kappa = 0$	$\kappa = 1 (\times 4)$	$\kappa = \sqrt{2} (\times 4)$	$\kappa = 2 (\times 4)$	$\kappa = \sqrt{5} (\times 8)$	$\kappa = 2\sqrt{2} (\times 4)$	Denomination
$\tilde{E}/c$	0						1
	1.28						$\sigma_T$
	4.71						$\varepsilon_T$
	8.77	6.79					$\sigma_T + \Delta\kappa$
		9.52		9.44			$\sigma'_T$
	12.9		11.6				$\varepsilon_T + \Delta\kappa$
	14.1	13.6			13.15		
	14.4				13.5		
			14.5				
			15.6				
		16.0				14.67	
		17.3				15.4	
				17.6			
	17.7						
	17.9		18.4				
						18.46	

TABLE II. Low-energy spectrum  $\tilde{E}/c = (E - E_0)\sqrt{N}/c$  for the Ising QFT with  $\tau = i$  obtained from ED/QMC on the square lattice.  $c$  denotes the speed of light (see Tab. I). Unshaded (shaded) cells are even (odd) under spin-inversion. Blue colored values are obtained from QMC+ED, the other values from ED alone. The degeneracy of the finite-momentum levels is given in brackets, all levels for  $\kappa = 0$  are not degenerate, some very close levels may, however, be actually degenerate in the thermodynamic limit. The given values are obtained by linear fits of the finite-size levels  $\tilde{E}_N/c$  as a function of  $1/N$  and should be accurate up to variations of the last given digit. Obtaining more precise values is a non-trivial task as the values from QMC are the result of a series of fits and ED data shows larger finite-size effects for higher levels in the spectrum and for larger momentum  $\kappa$ , where the available finite-size momenta already lie within the non-linear regime of the dispersion relation close to the Brillouin zone boundary. The last column shows our denomination of the levels as it was used in the main text. See Tab. III for a comparison with  $\epsilon$ -expansion results.

$\tau = i$	$\kappa = 0$	$\kappa_2 = 0$	$\kappa = 1$	$\kappa = \sqrt{2}$	$\kappa_2 = \sqrt{2}$	$\kappa = 2$	$\kappa = \sqrt{5}$	$\kappa = 2\sqrt{2}$	Denomination
$\tilde{E}/c$	0								1
	1.825								$\sigma_T$
	5.16								$\varepsilon_T$
		6.40							$\sigma_T + \Delta\kappa$
		8.88							$\varepsilon_T + \Delta\kappa$
			9.01						
			11.35						
				12.41					
					14.867				
						12.95			
	13.39	12.95				12.95			
			15.51				14.873		
				16.00			15.83		
				16.50				15.51	
					16.00			16.32	
									17.78

TABLE III. Low-energy spectrum for the Ising QFT with modular parameter  $\tau = i$  from  $\epsilon$ -expansion. The notation  $\kappa_2$  indicates "two-particle" states (but this distinction loses meaning for higher  $\kappa$ ).

**Appendix E: Complete low-energy spectrum for Ising CFT with modular parameter  $\tau = \frac{1}{2} + \frac{\sqrt{3}}{2}i$** 

$\tau = \frac{1}{2} + \frac{\sqrt{3}}{2}i$	$\kappa = 0$	$\kappa = 1 (\times 6)$	$\kappa = \sqrt{3} (\times 6)$	$\kappa = 2 (\times 6)$	$\kappa = \sqrt{7} (\times 12)$	Denomination
	0					1
	1.35					$\sigma_T$
	5.03					$\varepsilon_T$
	9.33		7.77			$\sigma_T + \Delta\kappa$
	14.5		10.53			$\sigma'_T$
	15.1 ( $\times 2$ )		14.8	13.14		$\varepsilon_T + \Delta\kappa$
	18.3		16.1	14.6		
	19.8 ( $\times 2$ )				15.10	
					15.9	
					16.2	
				16.7		
				18.6		
					19.82	

TABLE IV. Low-energy spectrum for the Ising QFT with  $\tau = \frac{1}{2} + \frac{\sqrt{3}}{2}i$  obtained from ED/QMC on the triangular lattice. See Tab. II for further details and Tab. V for a comparison with  $\epsilon$ -expansion results.

$\tau = \frac{1}{2} + \frac{\sqrt{3}}{2}i$	$\kappa = 0$	$\kappa = 1 (\times 6)$	$\kappa = \sqrt{3} (\times 6)$	$\kappa = 2 (\times 6)$	$\kappa = \sqrt{7} (\times 12)$	Denomination
	0					1
	1.96					$\sigma_T$
	5.55					$\varepsilon_T$
	9.72		7.38			$\sigma_T + \Delta\kappa$
	14.31		10.02			$\sigma'_T$
	14.44		13.83	12.68		$\varepsilon_T + \Delta\kappa$
	15.23		14.90			
	16.66		14.90	14.54		
	17.59		15.08	14.67		
	18.13			16.96		
	18.24			17.97		
	19.61		18.84		19.28	

TABLE V. Low-energy spectrum for the Ising QFT with modular parameter  $\tau = \frac{1}{2} + \frac{\sqrt{3}}{2}i$  from  $\epsilon$ -expansion.

**Appendix F: Complete low-energy spectrum for Ising\* CFT with  $\tau = i$** 

$\tau = i$	(P,P)			(P,A)/(A,P)			(A,A)			Denomination
	$\kappa = 0$	$\kappa = 1$	$\kappa = \sqrt{2}$	$\kappa = 0$	$\kappa = 1$	$\kappa = \sqrt{2}$	$\kappa = 0$	$\kappa = 1$	$\kappa = \sqrt{2}$	
$\tilde{E}/c$	0			0.45			0.62			1
	4.71			8.5	7.3		9.0			$1'_T$
		9.52			10.4	11.4		10.3	9.6	$1''_T$
			11.6							$\varepsilon_T$

TABLE VI. Low-energy spectrum for the Ising\* CFT with  $\tau = i$  obtained from ED on the square lattice. The four distinct topological sectors are indicated by the corresponding boundary conditions (P,A) etc. in the two directions around the torus, where A(P) denotes (anti-)periodic boundary conditions (See main text for further details). The four lowest-lying levels constitute the topological four-fold degenerate groundstate manifold in the Toric Code phase and are still remarkably low in energy at criticality. See Tab. VII for a comparison with  $\epsilon$ -expansion results and Tab. II for further details.

$\tau = i$	(P,P)			(P,A)/(A,P)			(A,A)			Denomination
	$\kappa = 0$	$\kappa = 1$	$\kappa = \sqrt{2}$	$\kappa = 0$	$\kappa = 1$	$\kappa = \sqrt{2}$	$\kappa = 0$	$\kappa = 1$	$\kappa = \sqrt{2}$	
$\tilde{E}/c$	0			0.19			0.35			1
	5.16			7.54	6.88		9.75	9.75	9.18	$1'_T$
		8.88								$1''_T$
			11.35							$\varepsilon_T$

TABLE VII. Low-energy spectrum for the Ising\* CFT with  $\tau = i$  obtained from  $\epsilon$ -expansion.